Direct Model Predictive Current Control Strategy of Quasi-Z-Source Inverters

Ayman Ayad, *Student Member, IEEE*, Petros Karamanakos, *Member, IEEE*,
and Ralph Kennel, *Senior Member, IEEE*

***Abstract*—This paper presents a direct model predictive current control (MPC) strategy for quasi-Z-source inverters (qZSIs). A discrete-time model is derived that accurately captures all operating modes of the converter. Both sides of the qZSI are controlled simultaneously based on the inductor current and capacitor voltage on the dc side as well as the output current on the ac side. To improve the closed-loop performance of the converter a long prediction horizon is implemented. However, the underlying optimization problem may become computationally intractable because of the substantial increase in the computational power demands, which in turn would prevent the implementation of the control strategy in real time. To overcome this and to solve the problem in a computationally efficient manner, a branch-and-bound strategy is used along with a move blocking scheme. Simulation and experimental results are provided to verify the effectiveness of the presented control strategy.**

***Index Terms*—Quasi-Z-source inverter, model predictive control (MPC), long prediction horizon, branch-and-bound, move blocking**

I. Introduction

THE Z-source inverter (ZSI) was proposed in 2002 as an alternative to the traditional dc-ac converter. The ZSI fulfills the buck-boost function in a single-stage converter by utilizing a Z-source network, consisting of two identical inductors, two identical capacitors, and a diode [2], [3]. By employing an extra switching state, called *shoot-through state*, the ZSI can boost the input dc voltage to the desired dc-link voltage [4]. In comparison with the traditional two-stage inverter (consisting of a dc-dc boost converter and a voltage source inverter), the ZSI has a better efficiency, simpler design, and reduced cost [5], [6]. The quasi-Z-source inverter (qZSI) was presented as an improved version of the classical ZSI [7]. It has many additional advantages such as continuous input current and joint earthing of the dc source and the dc-link bus. Moreover, the voltage of one of the quasi-Z-source network capacitors is significantly reduced resulting in a smaller passive components size [8]. Taking into account the aforementioned characteristics, the qZSI can be considered as an attractive candidate for several power electronics applications, including photovoltaic applications [9]–[11].

Using traditional linear control techniques to control the qZSI appears to be a challenging task. The main reason is that the capacitor voltage (the dc-link voltage) and the inductor current on the dc side of the converter have to be controlled at the same time with the current/voltage on the ac side [10], [12]–[14]. Hence, separate control loops are required for the dc and ac sides. In addition, the dc side of the qZSI exhibits a nonminimum phase characteristic which requires much attention in the controller design in order to minimize its effect on the converter operation at different operating points. Moreover, the interacting between the dc- and the ac-side controllers should be avoided in order to ensure a satisfying performance for both sides of the qZSI [10], [11]. As an alternative, nonlinear control algorithms such as sliding mode control [15] and neural network control [16] have been applied to ZSI/qZSI. In comparison with the traditional proportional-integral (PI) based controllers, these algorithms exhibit fast dynamic behavior, at the expense though of again increased design complexity.

Over the last decade, model predictive control (MPC) [17] has been established as an attractive control algorithm for power electronics applications [18], [19]. Particularly, the so called *direct* MPC—also referred to as finite control set (FCS) MPC—has been extensively used, thanks to its design simplicity; the switches of the converter are directly manipulated without requiring a modulator [18], [20], [21]. Moreover, MPC, in general, and direct MPC, in particular, have been proved to be particularly effective when multiple-input, multiple-output (MIMO) systems with nonlinear, complex dynamics are concerned. The reason is that all the control objectives can be tackled in one stage since they are incorporated in one performance criterion, i.e. the cost function.

Motivated by the complexity of the qZSI and the above-mentioned advantages of MPC, a few research works have been recently published focusing on MPC for ZSI/qZSI, see e.g. [22]–[29]. It is worth mentioning, though, that in these works MPC is used in its simplest form, akin to a dead-beat controller. Specifically, a one-step horizon MPC is implemented, the goal of which is to eliminate the output error as fast and as much as possible within this short horizon. This forces the controller to take aggressive actions which may cause stability problems. For instance, short-horizon MPC cannot always deal with the nonminimum phase nature of the dc side of the qZSI. More specifically, due to the reverse capacitor voltage response during transients, a sufficiently long prediction horizon is required so that the controller can accurately predict not only that initial adverse system behavior, but also beyond that. In other words, the MPC scheme should be able to "see" beyond the initial reverse-response system behavior in order to ensure closed-loop stability.

As a consequence, the short-horizon MPC is not always sufficient to achieve a good system performance, especially when applied to complex systems such as the qZSI. Recent

A. Ayad and R. Kennel are with the Chair of Electrical Drive Systems and Power Electronics, Technische Universität München, Munich 80333, Germany (e-mail: ayman.francees@tum.de; ralph.kennel@tum.de).

P. Karamanakos is with the Department of Electrical Engineering, Tampere University of Technology, Tampere 33101, Finland (e-mail: p.karamanakos@ieee.org).

A preliminary version of this paper was presented at the IEEE International Symposium on Predictive Control of Electrical Drives and Power Electronics, Valparaíso, Chile, 2015, see [1].

works, such as [30]–[32] have shown that long-horizon MPC can significantly improve the system performance by reducing the current total harmonic distortion (THD). Moreover, apart from a very few cases (see [33, Chap. 10] and references therein for a short discussion), in the one-step horizon MPC formulations the switching effort penalization is not taken into account which is in contrast to the optimal control paradigm [17]. As a result, the switching frequency is not directly controlled, but merely an upper bound is imposed on it, as defined by the sampling interval[1]. This implies that the converter operates at the highest achievable switching frequency which in turn leads to high switching losses.

In this paper a long-horizon direct MPC algorithm—implemented as a current controller—is adopted to handle the multiple control objectives, i.e. the regulation of the output current, the inductor current, and the capacitor voltage to their reference values. A discrete-time model of the converter is derived, on which the controller relies to accurately predict the future behavior of the system over the whole operating regime. Besides, a long horizon is implemented so as to achieve an improved performance and to avoid the issues mentioned above. Nevertheless, since the computational complexity grows exponentially with the length of the prediction horizon, strategies need to be employed that balance the trade-off between the length of the prediction horizon and the number of computations required. To keep the computational complexity modest, a branch-and-bound technique [34] is employed and it is combined with a move blocking scheme [35] that yields a nontrivial prediction horizon.

This paper is structured as follows. In Section II, the continuous- and discrete-time models of the qZSI are derived. The optimization problem underlying MPC is formulated and solved in Section III. Next, for comparison purposes, a conventional PI-based controller is designed in Section IV. In Section V simulation results are presented, and in Section VI the proposed control strategy is experimentally tested. Section VII draws the conclusion.

II. Mathematical Model of the Quasi-Z-Source Inverter

Fig. 1 shows the configuration of the qZSI consisting of a quasi-Z-source network, a three-phase two-level inverter, and an RL load. With the inductors, L_1, L_2, the capacitors, C_1, C_2, and the diode D, the qZSI manages to boost the input voltage v_{in} to the desired dc-link voltage v_{dc}. This is done by including the extra shoot-through state. Consequently, the qZSI has two types of operating states, namely the non-shoot-through—comprising of the six active and two zero states of the conventional two-level voltage source inverter—and the shoot-through states, see Fig. 2[2].

Since the qZSI operates in different states, the associated models will be derived separately. Note that to simplify the

[1]The authors are aware of only one exemption, namely [22], in which the switching frequency of the ZSI/qZSI is directly controlled with MPC. However, this is not done by penalizing the switching effort, but by adding a switching frequency error term (i.e. the difference between the converter switching frequency and a desired one) to the objective function. Therefore, the formulated optimization problem underlying MPC violates the optimal control paradigm and a smooth transition between consecutive switching transitions is not guaranteed.

[2]In Fig. 2, NST stands for non-shoot-through and i_{ST} denotes the shoot-through current (i.e. the dc-link current during the shoot-through state).

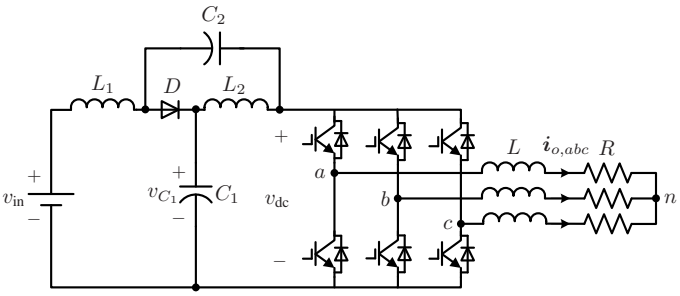

Fig. 1: Topology of the quasi-Z-Source Inverter (qZSI).

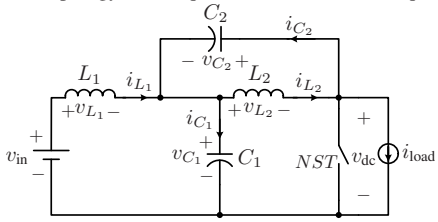

(a) Non-shoot-through state.

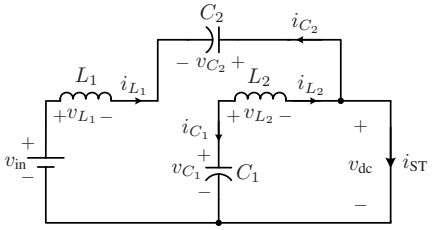

(b) Shoot-through state.

Fig. 2: Operation states of the qZSI.

modeling and to ease the computations, the variables are expressed in the stationary orthogonal system $(\alpha\beta)$ instead of the three-phase system (abc). Therefore, a variable $\boldsymbol{\xi}_{abc} = [\xi_a \ \xi_b \ \xi_c]^T$ in the abc system is transformed to a variable $\boldsymbol{\xi}_{\alpha\beta} = [\xi_\alpha \ \xi_\beta]^T$ in the $\alpha\beta$ system through $\boldsymbol{\xi}_{\alpha\beta} = \boldsymbol{K}\boldsymbol{\xi}_{abc}$,[3] where $\boldsymbol{K}$ is the Clarke transformation matrix

$$\boldsymbol{K} = \frac{2}{3}\begin{bmatrix} 1 & -\frac{1}{2} & -\frac{1}{2} \\ 0 & \frac{\sqrt{3}}{2} & -\frac{\sqrt{3}}{2} \end{bmatrix}. \tag{1}$$

The system states include the output current, the inductor currents, and the capacitor voltages. Thus, the state vector is $\boldsymbol{x} = [i_{o,\alpha} \ i_{o,\beta} \ i_{L_1} \ i_{L_2} \ v_{C_1} \ v_{C_2}]^T \in \mathbb{R}^6$. The three-phase switch position $\boldsymbol{u}_{abc} \in \mathcal{U}^3$ is considered as the input to the system, with $\boldsymbol{u}_{abc} = [u_a \ u_b \ u_c]^T$ and $\mathcal{U} = \{0, 1\}$. Moreover, the input voltage is considered as a disturbance to the system, i.e. $\boldsymbol{w} = v_{\text{in}} \in \mathbb{R}$.

As far as the output of the system is concerned, the output and the inductor currents along with the capacitor voltage are considered as the output variables, i.e. $\boldsymbol{y} = [i_{o,\alpha} \ i_{o,\beta} \ i_{L_1} \ v_{C_1}]^T \in \mathbb{R}^4$.

A. Non-Shoot-Through State

As can be seen in Fig. 2(a), at non-shoot-through state the diode is conducting, thus the input voltage source and the inductors deliver energy to the capacitors and the load. Accordingly, the system model is given by

$$\frac{\mathrm{d}\boldsymbol{x}(t)}{\mathrm{d}t} = \boldsymbol{F}_1\boldsymbol{x}(t) + \boldsymbol{G}_1\boldsymbol{u}_{abc}(t) + \boldsymbol{H}\boldsymbol{w}(t) \tag{2a}$$

$$\boldsymbol{y}(t) = \boldsymbol{E}\boldsymbol{x}(t)\,, \tag{2b}$$

[3]To this end, the subscript for vectors in the $\alpha\beta$ plane is dropped to simplify the notation. Vectors in the abc plane are denoted with the corresponding subscript.

where[4]

$$\boldsymbol{F}_1 = \begin{bmatrix} -\frac{R}{L} & 0 & 0 & 0 & 0 & 0 \\ 0 & -\frac{R}{L} & 0 & 0 & 0 & 0 \\ 0 & 0 & 0 & 0 & -\frac{1}{L_1} & 0 \\ 0 & 0 & 0 & 0 & 0 & -\frac{1}{L_2} \\ -\frac{\boldsymbol{u}_{abc}^T \boldsymbol{K}_{(:,1)}^{-1}}{C_1} & -\frac{\boldsymbol{u}_{abc}^T \boldsymbol{K}_{(:,2)}^{-1}}{C_1} & \frac{1}{C_1} & 0 & 0 & 0 \\ -\frac{\boldsymbol{u}_{abc}^T \boldsymbol{K}_{(:,1)}^{-1}}{C_2} & -\frac{\boldsymbol{u}_{abc}^T \boldsymbol{K}_{(:,2)}^{-1}}{C_2} & 0 & \frac{1}{C_2} & 0 & 0 \end{bmatrix}$$

$$\boldsymbol{G}_1 = \hat{v}_{\text{dc}} \begin{bmatrix} \frac{1}{L} & 0 \\ 0 & \frac{1}{L} \\ 0 & 0 \\ 0 & 0 \\ 0 & 0 \\ 0 & 0 \end{bmatrix} \boldsymbol{K}, \quad \boldsymbol{H} = \begin{bmatrix} 0 \\ 0 \\ \frac{1}{L_1} \\ 0 \\ 0 \\ 0 \end{bmatrix},$$

$$\boldsymbol{E} = \begin{bmatrix} 1 & 0 & 0 & 0 & 0 & 0 \\ 0 & 1 & 0 & 0 & 0 & 0 \\ 0 & 0 & 1 & 0 & 0 & 0 \\ 0 & 0 & 0 & 0 & 1 & 0 \end{bmatrix}.$$

where R (L) is the load resistance (inductance), and $\hat{v}_{\text{dc}}$ is the peak dc-link voltage, see appendix A.

B. Shoot-Through State

At shoot-through state the input voltage source and the capacitors charge the inductors, while the diode is cut-off, as shown in Fig. 2(b). During this state, the load is short-circuited since the upper and lower switches in at least one of the three phases are turned on simultaneously, i.e. $u_x = \bar{u}_x = 1$, where $\bar{u}_x$ denotes the position of the lower switch in phase $x \in \{a, b, c\}$. The converter at the shoot-through state is described by the following expression

$$\frac{\mathrm{d}\boldsymbol{x}(t)}{\mathrm{d}t} = \boldsymbol{F}_2 \boldsymbol{x}(t) + \boldsymbol{G}_2 \boldsymbol{u}_{abc}(t) + \boldsymbol{H}\boldsymbol{w}(t) \tag{3a}$$

$$\boldsymbol{y}(t) = \boldsymbol{E}\boldsymbol{x}(t)\,, \tag{3b}$$

where

$$\boldsymbol{F}_2 = \begin{bmatrix} -\frac{R}{L} & 0 & 0 & 0 & 0 & 0 \\ 0 & -\frac{R}{L} & 0 & 0 & 0 & 0 \\ 0 & 0 & 0 & 0 & 0 & \frac{1}{L_1} \\ 0 & 0 & 0 & 0 & \frac{1}{L_2} & 0 \\ 0 & 0 & 0 & -\frac{1}{C_1} & 0 & 0 \\ 0 & 0 & -\frac{1}{C_2} & 0 & 0 & 0 \end{bmatrix},$$

and $\boldsymbol{G}_2$ is the zero matrix of appropriate dimensions. It is worthwhile to mention that, as can be deduced from (3), the qZSI in shoot-through state can be considered as an autonomous linear dynamical system with an external disturbance.

C. Continuous-Time Model

Models (2) and (3) can be combined in one model that precisely describes the different operating states of the qZSI. To do so, an auxiliary binary variable d_{aux} is introduced. This variable indicates the state at which the converter operates, i.e.

$$d_{\text{aux}} = \begin{cases} 0 & \text{if non-shoot-through state (active or zero state)} \\ 1 & \text{if shoot-through state} \end{cases} \tag{4}$$

[4]For a matrix $\boldsymbol{M}$, $\boldsymbol{M}_{(:,i)}$ denotes its ith column.

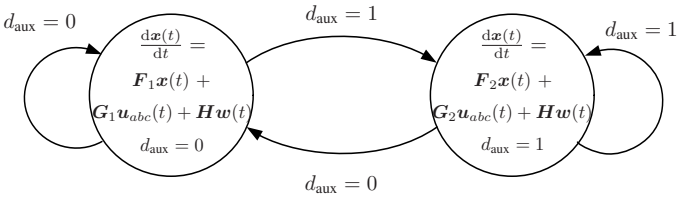

Fig. 3: The qZSI presented as a continuous-time automaton.

Since the transition from non-shoot-through state to shoot-through state, and vice versa, is input-dependent, (4) can be written as

$$d_{\text{aux}} = \begin{cases} 0 & \text{if } u_x \neq \bar{u}_x \forall\, x \in \{a, b, c\} \\ 1 & \text{if } \exists\, x \in \{a, b, c\} \text{ s.t. } u_x = \bar{u}_x = 1 \end{cases}. \tag{5}$$

Taking all the above into account, the model of the converter can be written as

$$\frac{\mathrm{d}\boldsymbol{x}(t)}{\mathrm{d}t} = \boldsymbol{F}\boldsymbol{x}(t) + \boldsymbol{G}\boldsymbol{u}_{abc}(t) + \boldsymbol{H}\boldsymbol{w}(t) \tag{6a}$$

$$\boldsymbol{y}(t) = \boldsymbol{E}\boldsymbol{x}(t)\,, \tag{6b}$$

where

$$\boldsymbol{F} = \begin{bmatrix} -\frac{R}{L} & 0 & 0 & 0 & 0 & 0 \\ 0 & -\frac{R}{L} & 0 & 0 & 0 & 0 \\ 0 & 0 & 0 & 0 & \frac{d_{\text{aux}}-1}{L_1} & \frac{d_{\text{aux}}}{L_1} \\ 0 & 0 & 0 & 0 & \frac{d_{\text{aux}}}{L_2} & \frac{d_{\text{aux}}-1}{L_2} \\ \frac{m_1}{C_1} & \frac{m_2}{C_1} & \frac{1-d_{\text{aux}}}{C_1} & -\frac{d_{\text{aux}}}{C_1} & 0 & 0 \\ \frac{m_1}{C_2} & \frac{m_2}{C_2} & -\frac{d_{\text{aux}}}{C_2} & \frac{1-d_{\text{aux}}}{C_2} & 0 & 0 \end{bmatrix}$$

and

$$m_1 = (d_{\text{aux}} - 1)\boldsymbol{u}_{abc}^T \boldsymbol{K}_{(:,1)}^{-1}, \quad m_2 = (d_{\text{aux}} - 1)\boldsymbol{u}_{abc}^T \boldsymbol{K}_{(:,2)}^{-1}$$

Moreover, $\boldsymbol{G} = (1 - d_{\text{aux}})\boldsymbol{G}_1$.

In Fig. 3 the qZSI represented as an automaton is depicted. As can be seen, the transition from one condition to another is specified by the auxiliary variable d_{aux}.

D. Internal Control Model

Using forward Euler approximation[5], the continuous-time model derived in Section II-C is discretized. The resulting state-space model of the qZSI in the discrete-time domain is of the form

$$\boldsymbol{x}(k+1) = \boldsymbol{A}\boldsymbol{x}(k) + \boldsymbol{B}\boldsymbol{u}_{abc}(k) + \boldsymbol{D}\boldsymbol{w}(k) \tag{7a}$$

$$\boldsymbol{y}(k) = \boldsymbol{C}\boldsymbol{x}(k)\,, \tag{7b}$$

with $\boldsymbol{A} = (\boldsymbol{F} + \boldsymbol{I})T_s$, $\boldsymbol{B} = \boldsymbol{G}T_s$, $\boldsymbol{D} = \boldsymbol{H}T_s$ and $\boldsymbol{C} = \boldsymbol{E}$. Moreover, $\boldsymbol{I}$ denotes the identity matrix, T_s is the sampling interval, and $k \in \mathbb{N}$.

III. Direct Model Predictive Control With Reference Tracking

A. Control Objective

For the qZSI, the control objective is twofold. First, the output current $\boldsymbol{i}_o$ should accurately track its reference value $\boldsymbol{i}_{o,\text{ref}}$. In addition, the inductor current i_{L_1} and the capacitor voltage v_{C_1} should be regulated along their reference

[5]Forward Euler approximation is adequately precise when a sampling interval of one to two tens of microseconds is used. For larger sampling intervals, exact discretization should be used instead.

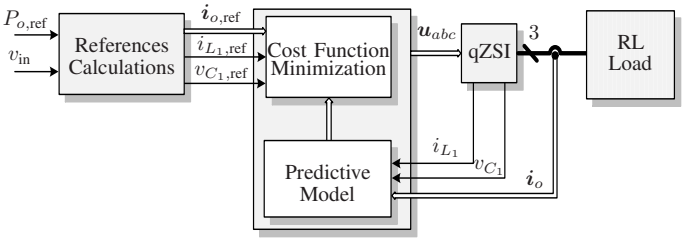

Fig. 4: Direct model predictive control with reference tracking for the qZSI.

trajectories $i_{L_1,\text{ref}}$ and $v_{C_1,\text{ref}}$, derived from an outer loop based on a power balance equation. Moreover, the switching losses are to be kept relatively low, which can be achieved indirectly by controlling the switching frequency[6]. Finally, during transients, the above-mentioned controlled variables should reach their desired values as fast and with as little overshoot as possible.

B. Controller Block Diagram

The block diagram of the proposed direct predictive controller with current reference tracking is illustrated in Fig. 4. As can be seen, the desirable system performance is achieved by directly manipulating the inverter switches, without the presence of a modulator. The proposed MPC algorithm first computes the evolution of the plant over the prediction horizon (i.e. the trajectories of the variables of concern) based on the measurements of the output current, inductor current, and capacitor voltage. Following, the optimal control action (i.e. the switching signals) is chosen by minimizing a performance criterion in real time.

C. Optimal Control Problem

At time-step k, the cost function that penalizes the error of the output variables and the switching effort over the finite prediction horizon of N time steps is written as

$$J(k) = \sum_{\ell=k}^{k+N-1} ||\boldsymbol{y}_{\text{ref}}(\ell+1|k) - \boldsymbol{y}(\ell+1|k)||^2_{\boldsymbol{Q}} + ||\Delta \boldsymbol{u}_{abc}(\ell|k)||^2_{\boldsymbol{R}} . \tag{8}$$

In (8) $\boldsymbol{y}_{\text{ref}} \in \mathbb{R}^4$ is a vector encompassing the reference values of the controlled variables (the output current, inductor current, and capacitor voltage), i.e. $\boldsymbol{y}_{\text{ref}} = [i_{o,\alpha,\text{ref}} \quad i_{o,\beta,\text{ref}} \quad i_{L_1,\text{ref}} \quad v_{C_1,\text{ref}}]^T$. Moreover, the term $\Delta \boldsymbol{u}_{abc}(k) = \boldsymbol{u}_{abc}(k) - \boldsymbol{u}_{abc}(k-1)$ is added to control the inverter switching frequency by penalizing the switching transitions. Finally, the diagonal, positive semidefinite matrices $\boldsymbol{Q}$ and $\boldsymbol{R} \in \mathbb{R}^{4\times 4}$ are the weighting matrices[7] that set the trade-off between the overall tracking accuracy and the switching frequency. Note that the diagonal entries of $\boldsymbol{Q}$ are chosen such that the tracking accuracy among the three output variables is prioritized. More specifically, priority is given to the output current by penalizing the corresponding error more heavily. This is achieved by choosing larger values for the corresponding diagonal entries in $\boldsymbol{Q}$. This implies that when more weight is put into the tracking of the output current reference, then the trade-off between the overall tracking accuracy and the switching frequency is simplified to the trade-off between the output current THD and the switching frequency of the converter, given by

$$f_{\text{sw}} = \lim_{M\to\infty} \frac{1}{MT_s} \cdot \frac{1}{6} \sum_{\ell=0}^{M-1} \frac{1}{2} \Big(||\boldsymbol{u}_{abc}(\ell) - \boldsymbol{u}_{abc}(\ell-1)||_1 + ||\bar{\boldsymbol{u}}_{abc}(\ell) - \bar{\boldsymbol{u}}_{abc}(\ell-1)||_1 \Big) . \tag{9}$$

According to (9), the switching frequency is computed by counting the number of *on* switching transitions over a time interval and by dividing this number by the length MT_s of that interval. The *average* switching frequency is then obtained by averaging over the 6 controllable switches of the converter. Note that the first term of the summation $||\boldsymbol{u}_{abc}(\ell) - \boldsymbol{u}_{abc}(\ell-1)||_1$ would suffice if and only if the switches in phase $x \in \{a,b,c\}$ changed position in a complementary manner, i.e. when the upper switch was on the lower was off ($u_x = 1 \rightarrow \bar{u}_x = 0$), and vice versa ($u_x = 0 \rightarrow \bar{u}_x = 1$). However, since both switches in any phase leg can be simultaneously on, the second term of the summation, i.e. $||\bar{\boldsymbol{u}}_{abc}(\ell) - \bar{\boldsymbol{u}}_{abc}(\ell-1)||_1$, with $\bar{\boldsymbol{u}}_{abc} = [\bar{u}_a \ \bar{u}_b \ \bar{u}_c]^T$, is added so that the switching transitions during the shoot-through state are also considered; the case $u_x = \bar{u}_x = 1$ is not concealed. By introducing this term, though, the on transitions are counted twice (once with each term). To compensate for that, the summation is divided by 2.

The optimal sequence of control actions is then computed by minimizing the cost function (8) over the optimization variable, i.e. the switching sequence over the horizon $\boldsymbol{U}(k) = [\boldsymbol{u}^T_{abc}(k) \ \boldsymbol{u}^T_{abc}(k+1) \dots \boldsymbol{u}^T_{abc}(k+N-1)]^T$, i.e.

$$\begin{aligned} \underset{\boldsymbol{U}(k)}{\text{minimize}} \quad & J(k) \\ \text{subject to} \quad & \text{eq. (7)} \\ & \boldsymbol{U}(k) \in \mathbb{U} \ . \end{aligned} \tag{10}$$

with $\mathbb{U} = \mathcal{U}^{3N}$. Having found the optimal switching sequence $\boldsymbol{U}^*(k)$, only its first element $\boldsymbol{u}^*_{abc}(k)$ is applied to the qZSI, whereas the rest are discarded. At the next time-step $k+1$, the whole procedure is repeated with updated measurements over a one-step shifted horizon, as the receding horizon policy dictates [17].

D. Reducing the Computational Complexity

Problem (10) is in general computationally demanding due to the integer nature of the optimization variable. As already mentioned, its computational complexity increases exponentially with its size, i.e. the total number of candidate solutions for the problem under examination is 8^N. Therefore, it is likely that a relatively long prediction horizon—required for an improved system performance—would result in a problem that is computationally intractable. To reduce the increased computational burden and to manage to solve the underlying optimization problem (10) in real time in a matter of a few microseconds, heuristics and approximations are adopted in this work.

First, a branch-and-bound algorithm is implemented [34]. A depth-first search is performed on the generated search tree, the branches of which are the elements of the candidate solutions of (10), i.e. the elements $\boldsymbol{u}_{abc}(\ell), \forall\, \ell = k, \dots, k+N-1$ of the switching sequences $\boldsymbol{U}(k)$. Hence, the optimal solution

[6] As mentioned in Appendix A, the *average* switching frequency is controlled with direct MPC. For simplicity, the word *average* is dropped in the remainder of the paper.

[7] The squared norm weighted with the positive (semi)definite matrix $\boldsymbol{W}$ is given by $||\boldsymbol{\xi}||^2_{\boldsymbol{W}} = \boldsymbol{\xi}^T \boldsymbol{W} \boldsymbol{\xi}$.

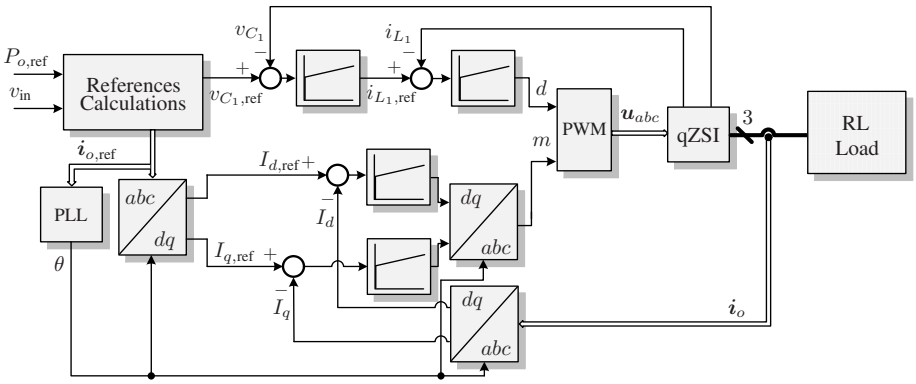

Fig. 5: Linear control with PWM for the qZSI.

is found by exploring each branch of the search tree as far as possible, i.e. until reaching a dead end or the bottom level, where backtracking occurs to explore unvisited nodes in higher levels. Having computed a good upper bound as soon as possible, then suboptimal branches can be pruned at the early stages of the search process, thus reducing the number of the candidate solutions. Furthermore, a branching heuristic is employed to warm-start the optimization procedure by starting from a "promising" branch, i.e. a branch that would lead to a tight upper bound. In particular, the first explored branch of the tree is the shifted by one time step previous solution $\boldsymbol{U}^*(k-1)$—in accordance with the receding horizon policy—concatenated with the last control action $\boldsymbol{u}^*(k+N-2)$.

To further reduce the computations required, while keeping the prediction horizon long enough, a move blocking technique [35], is utilized in this paper. The main idea of this technique is to split the prediction horizon into two segments, N_1 and N_2, where the total number of prediction steps is $N = N_1+N_2$, with $N_1, N_2 \in \mathbb{N}^+$. The first part of the horizon N_1 is finely sampled with the sampling interval T_s, while the second part N_2 is sampled more coarsely with a multiple of T_s, i.e. with $T_s' = n_s Ts$, where $n_s \in \mathbb{N}^+$. This results in a total prediction interval of $N_1 T_s + N_2 T_s' = (N_1 + n_s N_2)T_s$, thus, an adequate long prediction horizon is achieved using a few number of prediction steps [36], [37]. Using this technique, and in combination with the aforementioned branch-and-bound strategy, the calculation efforts can be dramatically decreased as shown in Section V.

In order to show how the overall control strategy works, the proposed direct MPC algorithm for the qZSI is described in appendix B.

IV. Conventional PI-Based Controller With PWM

Before evaluating the performance of the proposed MPC-based current control scheme, and for comparison purposes, a well-established linear controller is also implemented, see [4], [9], [10] and references therein. The block diagram is depicted in Fig. 5. As can be seen, PI controllers are used on each side of the qZSI. The aim of the dc-side controller is to boost the dc-link voltage. To achieve this, the dc-side controller is subdivided into two cascaded control loops[8]. The outer loop—the voltage controller—regulates the capacitor voltage v_{C_1} by adjusting the reference of the inductor current $i_{L_1,\text{ref}}$. The inner loop, i.e. the current controller, regulates the inductor current i_{L_1} by manipulating the shoot-through duty cycle d. On the ac side, the PI controller manipulates the inverter modulation index m in order to achieve tracking of the output current reference.

In a last step the shoot-through duty cycle d and the modulation index m are fed into the PWM block which generates the switching signals. As for the PWM techniques for the qZSI, there are three different methods in the literature: simple boost control, maximum boost control, and maximum constant boost control [2], [38], [39]. In this work, the simple boost control method with third harmonic injection is implemented because it introduces constant shoot-through duty cycle which in turn results in lower inductor current ripples.

[8]In order to have a fair comparison with the proposed MPC strategy, PI controllers are used to control both the capacitor voltage and the inductor current of the dc side.

V. Simulation Results

To investigate the performance of the proposed MPC scheme for the qZSI, several simulations using Matlab/Simulink have been conducted. The system parameters are chosen as $v_{\text{in}} = 70\,\text{V}$, $L_1 = L_2 = 1\,\text{mH}$, $C_1 = C_2 = 480\,\mu\text{F}$, $R = 10\,\Omega$, and $L = 10\,\text{mH}$. Based on the desired output power ($P_{o,\text{ref}} = 540\,\text{W}$), the output current reference $\boldsymbol{i}_{o,\text{ref}}$ $\left(= \sqrt{\frac{2P_{o,\text{ref}}}{3R}}\right)$ is set to 6 A, while the inductor current reference is equal to 7.7 A ($i_{L_1,\text{ref}} = P_{o,\text{ref}}/v_{\text{in}}$). In order to calculate the capacitor voltage reference, the following derivation is used. First, the output power P_o of the qZSI can be calculated by

$$P_o = \frac{3}{2}\,\hat{v}_o\,\hat{i}_o\,\cos\varphi\,, \tag{11}$$

where $\hat{v}_o$ ($\hat{i}_o$) is the peak output voltage (current) and $\cos\varphi$ is the system power factor which can be calculated from the load impedance. Thus, $\hat{v}_o$ can be written as

$$\hat{v}_o = \frac{2\,P_o}{3\,\hat{i}_o\,\cos\varphi}\,, \tag{12}$$

Using the output power and current reference values, and based on the load, (i.e. $P_{o,\text{ref}}$, $\boldsymbol{i}_{o,\text{ref}}$, and the RL load), the desired peak value of the output voltage is $\hat{v}_o = 64\,\text{V}$. In order not to affect the sinusoidal waveform of the output current and to prevent the interacting between the dc and ac sides, the capacitor voltage reference $v_{C_1,\text{ref}}$ should be greater than double the required peak output voltage [10]. Consequently, the capacitor voltage reference is chosen to be equal to 150 V, i.e. $v_{C_1,\text{ref}} = 2.3{\cdot}\hat{v}_o$. In the remainder of the paper the capacitor voltage reference is kept fixed at the aforementioned value in order to keep the peak dc-link voltage constant at 230 V, see (16).

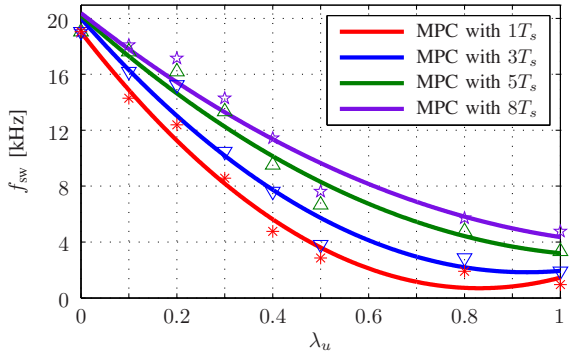

Fig. 6: The effect of the weighting factor (λ_u) on the switching frequency for the MPC with different prediction horizons ($1T_s$, $3T_s$, $5T_s$, and $8T_s$). The measurements are shown as (red) asterisks, (blue) downward-pointing triangles, (green) upward-pointing triangles, and (magenta) stars, referring to individual simulation results, when the system was controlled with MPC with prediction horizon intervals of $1T_s$, $3T_s$, $5T_s$ and $8T_s$, respectively. The data points were approximated using a second degree polynomial.

For the scenarios examined below, the converter operates at the desired switching frequency $f_{\text{sw}} \approx 5\,\text{kHZ}$, by setting $\boldsymbol{Q} = \text{diag}(1, 1, 0.1, 0.02)$ and $\boldsymbol{R} = \lambda_u \boldsymbol{I}$ in (8), where $\lambda_u > 0$ is appropriately chosen, by exploring the trade-off between λ_u and the switching frequency f_{sw}, as shown in Fig. 6. The sampling interval is chosen as $T_s = 25\,\mu\text{s}$.

A. Steady-State Performance

First, the effect of the prediction horizon length on the system performance is examined. The THD of the output current $I_{o,\text{THD}}$ is used as a performance metric. This is considered as a meaningful and informative metric during steady-sate operation since it quantifies the tracking performance of the controller.

Table I summarizes the output current THD $I_{o,\text{THD}}$ produced by the presented MPC current controller[9]. Regardless of the prediction horizon length, the converter operates at a switching frequency of $f_{\text{sw}} \approx 5\,\text{kHz}$. As can be seen in Table I, when longer prediction intervals are implemented the closed-loop system performance can be significantly improved. In particular, it can be observed that even a prediction interval of $4T_s$ can be considered long enough to achieve a noteworthy reduction in the current THD.

To further assess the performance of the proposed MPC strategy, the linear controller presented in Section IV is examined. Again, the converter operates at a switching frequency of $5\,\text{kHz}$ and under the same input/output operating conditions. It is found that the output current THD value is 8.30%. The current THD of the proposed MPC with a prediction interval of $3T_s$ (6.52%, see Table I) is lower than the one with the PI-based controller. These results confirm that long-horizon MPC definitely leads to better performance than the one with the conventional PI control.

In a next step, the trade-off between the current THD and the switching frequency is investigated. The switching frequency of the qZSI varies from $f_{\text{sw}} = 3$ to $f_{\text{sw}} = 15\,\text{kHz}$ by changing the value of the weighting factor λ_u, while keeping the entries of $\boldsymbol{Q}$ constant. For each switching frequency, the resulting $I_{o,\text{THD}}$ is recorded. The three-dimensional graphs that show the relationship among the weighting factor (λ_u), switching frequency (f_{sw}), and output current THD for MPC with different prediction horizons are shown in Fig. 7.

[9]Note that MPC with a prediction horizon of length $1T_s$ corresponds to the existing one-step horizon MPC.

TABLE I: Output current THD produced by the proposed MPC scheme depending on the length of the prediction horizon. The switching frequency is approximately $5\,\text{kHz}$.

Length of Prediction Horizon NT_s	Current THD $I_{o,\text{THD}}\%$
$1T_s$	16.09
$2T_s$	11.80
$3T_s$	6.52
$4T_s$	5.01
$5T_s$	3.65
$6T_s$	2.34
$7T_s$	1.99
$8T_s$	1.46

To further investigate the trade-off between the current THD and the switching frequency, the MPC algorithm is implemented with four different prediction horizon lengths ($1T_s$, $3T_s$, $5T_s$, and $8T_s$). For comparison purposes, the respective THD values produced by the linear controller are also included. The individual simulations—indicated by markers—are approximated by second and third degree polynomials in Figs. 8(a) and 8(b), respectively.

Fig. 8(a) verifies that long-prediction horizon MPC can remarkably decrease the current THD, especially when the switching frequency is relatively low. For example, at a switching frequency of $f_{\text{sw}} = 3\,\text{kHz}$, the current THD of the MPC with $1T_s$ prediction horizon is $I_{o,\text{THD}} = 19.23\%$. However, the THD highly reduces to 3.15% with an $8T_s$ prediction horizon. On the other hand, when higher switching frequencies are considered, the improvement in the current THD is still present. Furthermore, based on Fig. 8(a) it can be concluded that MPC with a prediction interval of $3T_s$ achieves a lower current THD than the PI-based control, and when the prediction interval extends to $8T_s$, it notably outperforms it.

This can also be observed in Fig. 8(b), where the *relative* current THD ($\delta_{\text{THD}}\%$) of the MPC strategy with the aforementioned prediction lengths is depicted versus the same range of switching frequencies. The relative current THD of the MPC is normalized to the THD resulting from the PI-based control and given in percent according to the following expression [32]

$$\delta_{\text{THD}} = \frac{\text{THD}_{\text{MPC}} - \text{THD}_{\text{PI}}}{\text{THD}_{\text{PI}}} \cdot 100\%. \tag{13}$$

Fig. 8(b) shows that the current THD produced by MPC with $1T_s$ horizon is higher by up to 100% for switching frequencies around $7\,\text{kHz}$, compared to that of a PI-based controller. Increasing the prediction horizon length to $8T_s$, the MPC produces currents with reduced THD values by about $70 - 80\%$ for switching frequencies between 3 and $15\,\text{kHz}$. These results point out that using MPC with longer horizon effectively improves the performance of the qZSI and introduces better behavior than the traditional PI control.

B. Discussion on Stability

As mentioned in Section I, the qZSI is a nonminimum system. More specifically, assuming a linearized model, the shoot-through duty cycle-to-capacitor voltage transfer function contains a right half-plane zero, implying that the sign of the gain is not always positive. Physically, this means that the system exhibits a reverse-response behavior during transients.

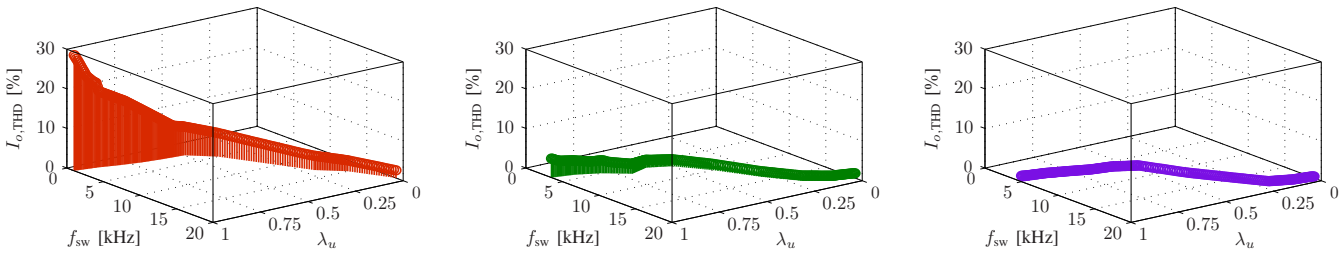

(a) MPC with $1T_s$ (b) MPC with $5T_s$ (c) MPC with $8T_s$

Fig. 7: The effect of the weighting factor (λ_u) on the switching frequency and the output current THD for the MPC with different prediction horizons ($1T_s$, $5T_s$, and $8T_s$).

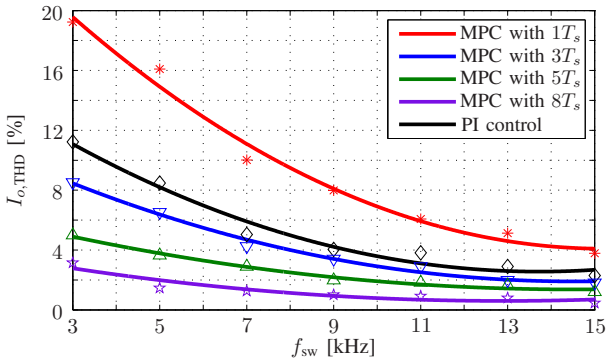

(a) Current THD and switching frequency.

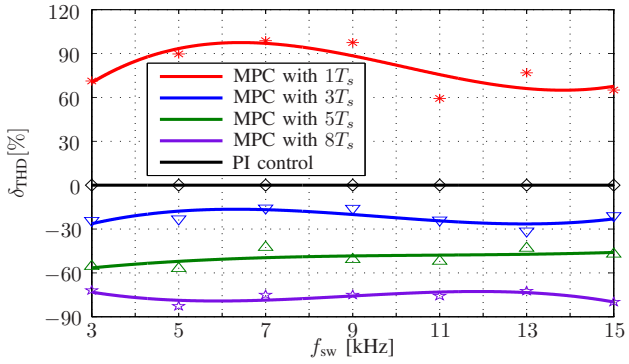

(b) Relative current THD and switching frequency.

Fig. 8: Trade-off between the output current THD $I_{o,\text{THD}}$ and the switching frequency f_{sw} for the PI-based controller and the MPC with prediction horizon length of $1T_s$, $3T_s$, $5T_s$, and $8T_s$.

For example, when the output power demands increase then the ac side needs to be instantaneously short circuited for a nonnegligible time for the dc-link voltage to remain at the desired level. This prolonged short-circuit situation of the ac side (which can be interpreted as an instantaneous increase in the shoot-through duty cycle) causes the capacitor voltage to initially drop and diverge from its reference value. A controller should be able to bring the voltage back to its predefined value in order to keep the system stable. As far as MPC is concerned, this means that the prediction horizon should be long enough, so that the controller can accurately predict the whole phenomenon and "see" beyond the initial voltage drop.

In order to show how long-horizon MPC can ensure stability under conditions single-step MPC fails to do, the following scenario is examined. The desired output power is stepped up at $t = 20\,\text{ms}$ from $P_{o,\text{ref}} = 135$ to $1215\,\text{W}$. Accordingly, the output current reference is changed from 3 to 9 A and the inductor current reference from 1.9 to 17.4 A (see beginning of Section V); for this test the capacitor voltage reference is kept fixed at 150 V. The qZSI is controlled with MPC with prediction intervals equal to $1T_s$ and $5T_s$. The simulation results are shown in Figs. 9 and 10, respectively. In both cases the switching frequency is set to approximately 5 kHz.

As can be seen in Figs. 9 and 10, before the demanded output power change the system behaves almost the same, regardless of the length of the prediction horizon. Nonetheless, MPC with a prediction interval of $5T_s$ produces lower current THD than single-step horizon MPC, as expected and explained in Section V-A. When the step change occurs at $t = 20\,\text{ms}$, MPC with horizon of $1T_s$ fails to track the reference values of the dc- and ac-side variables, see Fig. 9. On the other hand, long-horizon MPC manages to follow the changes in the reference values of the controlled variables and eliminates the resulting errors as fast as possible.

From the above-shown results it can be understood that short-horizon MPC fails to predict beyond the initial capacitor voltage drop. Thus, it computes a plan of control actions that is suboptimal; this plan does not suffice to bring the system back to steady-state operation after its initial reverse response; consequently it becomes unstable. Long-horizon MPC, however, manages to keep the system stable. The controller predicts within the $5T_s$ prediction horizon both the voltage drop at the beginning of the transient as well as its subsequent increase, and thus picks the corresponding sequence of control actions that achieve this.

C. Robustness Against Parameters Variation

MPC, as a model-based control strategy, relies on an accurate model of the examined system in order to come up with the best possible plan of control actions. MPC schemes for power electronics, though, are typically highly robust. The accuracy of the predictions is high since the models used in power electronics are fairly accurate, at least compared to other disciplines. Moreover, the receding horizon policy in MPC adds feedback and provides MPC with a high degree of robustness to model mismatches and disturbances. To verify this argument, in this section, the impact of parameter variations on the system performance is examined when MPC with a $5T_s$ prediction length is implemented.

In the first case, the resistive part R of the RL load is halved; at time $t = 20$ ms the resistor R is changed from 10 to $5\,\Omega$. The simulation results for the three controlled variables (the capacitor voltage, inductor current, and output current) are shown in Fig. 11. As can be seen, the three variables track their references effectively. However, the output current distortions become higher; the THD increases from 3.65 % to 4.39 %, see Fig. 11(c). In addition, the capacitor voltage and

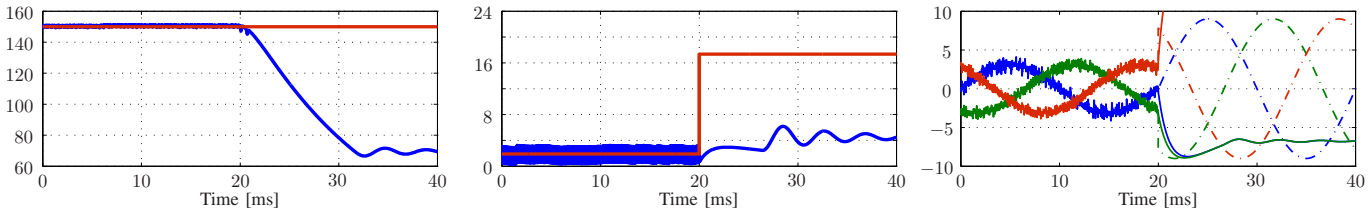

(a) Capacitor voltage v_{C_1} and its reference in [V] (b) Inductor current i_{L_1} and its reference in [A] (c) Three-phase output current $\boldsymbol{i}_o$ (solid lines) and their references (dash-dotted lines) in [A]

Fig. 9: Simulation results for a step change in the output current reference with MPC and a $1T_s$ prediction horizon length.

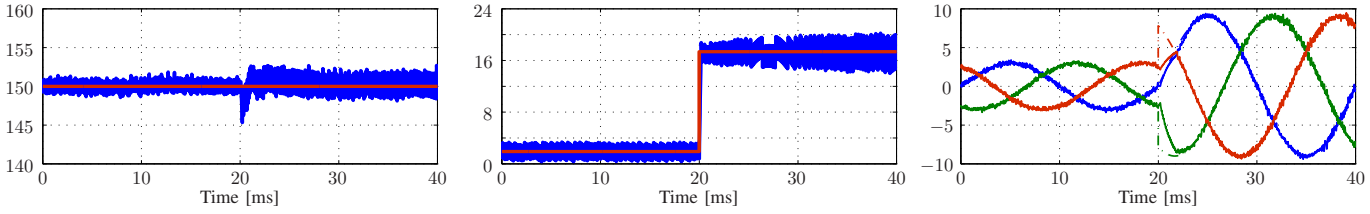

(a) Capacitor voltage v_{C_1} and its reference in [V] (b) Inductor current i_{L_1} and its reference in [A] (c) Three-phase output current $\boldsymbol{i}_o$ (solid lines) and their references (dash-dotted lines) in [A]

Fig. 10: Simulation results for a step change in the output current reference with MPC and a $5T_s$ prediction horizon length.

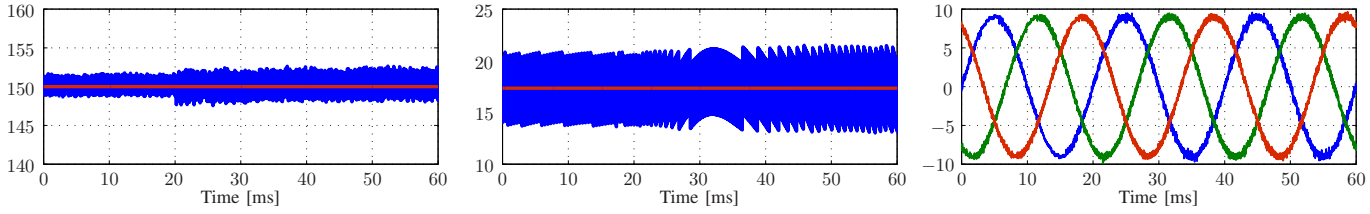

(a) Capacitor voltage v_{C_1} and its reference in [V] (b) Inductor current i_{L_1} and its reference in [A] (c) Three-phase output current $\boldsymbol{i}_o$ (solid lines) and their references (dash-dotted lines) in [A]

Fig. 11: Simulation results for MPC and a $5T_s$ prediction horizon length when R of the RL load is reduced by $50\,\%$.

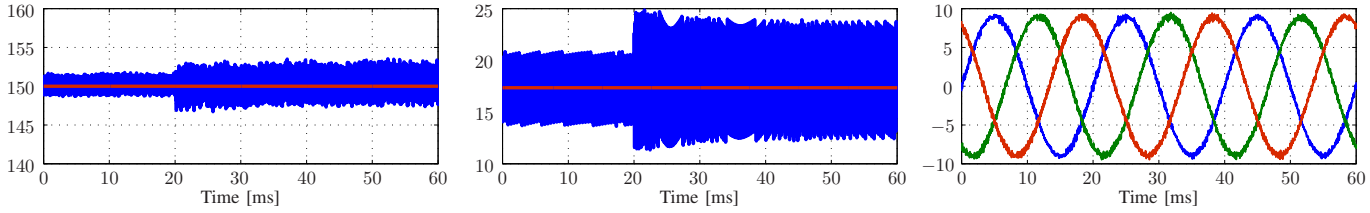

(a) Capacitor voltage v_{C_1} and its reference in [V] (b) Inductor current i_{L_1} and its reference in [A] (c) Three-phase output current $\boldsymbol{i}_o$ (solid lines) and their references (dash-dotted lines) in [A]

Fig. 12: Simulation results for MPC and a $5T_s$ prediction horizon length when L_1 and L_2 of the qZS network are reduced by $50\,\%$.

inductor current exhibit slightly higher ripples, see Figs. 11(a) and 11(b), respectively.

In the second test, the qZS network inductances (L_1 and L_2) are changed from their nominal values of 1000 mH to 500 mH. The simulation results for both sides are shown in Fig. 12. As can be observed in Fig. 12(c), the output current remains unaffected by this change on the dc side, since its THD is marginally increased by $2.3\,\%$. On the dc side, although the ripples of the capacitor voltage and the inductor current are more pronounced, the controlled variables are still regulated along their references and a zero steady-state error is achieved. These results confirm that—thanks to the receding horizon policy—MPC with long-horizon remains robust to parameter variations in the underlying prediction model.

D. Computational Burden

Since an increased prediction horizon entails a subsequent increase in the computational complexity of the MPC algorithm, the latter is investigated in this section. This is done in terms of the complete switching sequences $\boldsymbol{U}$ and the nodes being evaluated at each time-step to obtain the optimal solution.

Table II shows the average and the maximum number of the sequences μ and nodes ν examined as a function of the length of the prediction horizon. To highlight the computational efficiency of the proposed MPC algorithm, the number of the switching sequences evaluated with the exhaustive enumeration algorithm—typically used in the field of power electronics to solve MPC problems of the form (10) [18]—is also presented. As can be seen, thanks to the branch-and-bound scheme and the move blocking strategy, the number of examined sequences is significantly reduced. For instance, for a prediction horizon of $6T_s$ total length[10] the maximum number of sequences—which is of importance for a real-time implementation since it corresponds to the worst-case scenario—is reduced by about 99.96%. In addition, the maximum number of the visited nodes is reduced by about 99.95%. The significant reduction in the required calculations enables

[10]The $6T_s$ prediction horizon length is achieved with the proposed MPC strategy by setting $N_1 = 2$, $N_2 = 2$, $n_s = 2$ in the move blocking scheme, see Section III-D.

TABLE II: Average and maximum numbers of examined switching sequences μ and nodes ν depending on the length of the prediction horizon.

Length of Prediction Horizon $NT_s = (N_1 + n_s N_2)T_s$	Exhaustive Search			Proposed MPC Strategy				
	$N_1 + N_2$	μ	ν	$N_1 + N_2$	avg(μ)	avg(ν)	max(μ)	max(ν)
$1T_s$	$1+0$	8	8	$1+0$	8	8	8	8
$2T_s$	$2+0$	64	72	$2+0$	16.4	25.3	24	32
$3T_s$	$3+0$	512	584	$1+1$	23.2	33.4	32	44
$4T_s$	$4+0$	4,096	4,680	$2+1$	41.7	56.2	64	87
$5T_s$	$5+0$	32,768	37,448	$1+2$	56.5	75.9	80	100
$6T_s$	$6+0$	262,144	299,592	$2+2$	78.1	99.6	104	126
$7T_s$	$7+0$	2,097,152	2,396,744	$1+3$	84.6	111.4	112	147
$8T_s$	$8+0$	16,777,216	19,173,960	$2+3$	114.2	153.8	152	188

the proposed MPC to be implemented in real time as shown in Section VI.

VI. Experimental Results

Experiments for the qZSI with both the proposed MPC scheme and the linear PI-based controller were carried out in the laboratory. The system parameters are the same as in Section V. The controllers were implemented on a low-cost, low-power field programmable logic array (FPGA) Cyclone III-EP3C40Q240C8, with 39,600 logic elements, 126 multipliers, and 1,161,216 total RAM bits. To compensate for the time delay introduced by the MPC controller, a delay compensation strategy is applied [40]. The complete experimental set-up is displayed in Fig. 13.

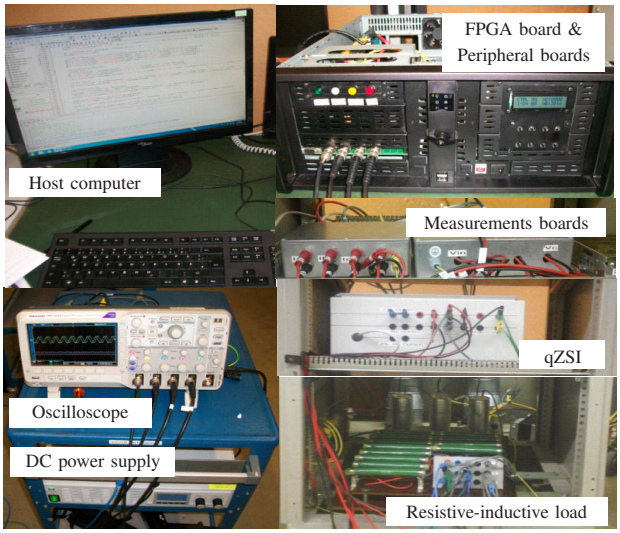

Fig. 13: System set-up in the laboratory.

A. Steady-State Operation

The first scenario examined is that of the steady-state behavior of the qZSI when operated at a switching frequency of $\approx 5\,\text{kHz}$, as computed over 50 fundamental periods, i.e. by setting $M = 40{,}000$ in (9). As far as the MPC scheme is concerned, two different prediction horizon lengths are tested, i.e. $1T_s$ and $5T_s$, with the weighting factor λ_u being 0.42 and 0.75, respectively, in order to achieve the desired switching frequency (see Fig. 6). Considering the parameters of the PI controllers, they are tuned such that no steady-state error appears when operating under nominal conditions, while current regulation with as little overshoot as possible is achieved. By using the concept of averaging, the closed-loop transfer function of the linearized system is first derived (see [10], [14]), and then by utilizing the Routh-Hurwitz stability criterion, the parameters of the PI controllers chosen. Therefore, the gains of the dc-side controllers are chosen to be $k_{p_c} = 0.008$ and $k_{i_c} = 0.05$ for the outer PI voltage control loop and $k_{p_i} = 0.03$ and $k_{i_i} = 0.2$ for the inner PI current control loop. As for the ac-side, the control parameters are chosen as $k_{p_1} = k_{p_2} = 0.05$ and $k_{i_1} = k_{i_2} = 30$.

The experimental results obtained with the MPC are shown in Figs. 14, 15, 16 and 17, whereas those produced by the PI control are illustrated in Figs. 18 and 19. Concretely, the results related to the dc side of the converter are illustrated in Figs. 14 and 16 for the MPC with $1T_s$ and $5T_s$ prediction horizon lengths, respectively, and in Fig. 18 for the linear controller. The respective ac-side results are shown in Figs. 15 and 17 for the MPC, and Fig. 19 for the PI-based controller.

With regard to the dc side, it can be observed that the inductor current accurately tracks its reference in all cases examined (Figs. 14(b), 16(b), and 18(b)), resulting in a boosted capacitor voltage $v_{C_1} = 150\,\text{V}$ (Figs. 14(a), 16(a), and 18(a)) and a peak dc-link voltage of $\hat{v}_{\text{dc}} = 230\,\text{V}$ (Figs. 14(c), 16(c), and 18(c)). Regardless of the prediction horizon, the MPC shows good steady-state behavior with low inductor current ripples. On the other hand, the inductor current and capacitor voltage ripples are slightly higher with the PI-based controller.

On the ac side of the converter, the tracking accuracy of the proposed controller is not affected by the shoot-through state as can be seen in Figs. 15(a) and 17(a) where the three-phase output currents are depicted along with their references. Furthermore, the MPC with a $5T_s$ prediction interval produces THD $I_{o,\text{THD}} = 4.65\%$ (see Fig. 17(b)), significantly lower than the one resulting from the $1T_s$ horizon MPC, which is 17.05% (see Fig. 15(b)). This confirms that increasing the prediction horizon improves the system performance as far as the output current THD is concerned, as also shown in Section V. With the PI-based controller the current THD is 8.95% (see Fig. 19(b)) which is notably higher than that of the MPC with horizon length $5T_s$. These results are in line with the simulation ones.

It can be concluded that the overall performance of the qZSI is improved with MPC when a longer horizon is used. By utilizing the branch-and-bound and move blocking techniques, the computationally burden is reduced and the MPC algorithm can be successfully implemented in the FPGA. Without adding any outer loops that would complicate the controller design, the proposed MPC algorithm outperforms the PI-based controller.

B. Current THD and Switching Frequency

Some experiments were conducted to study the trade-off between the current THD and the switching frequency of the proposed MPC strategy with prediction intervals equal to $1T_s$,

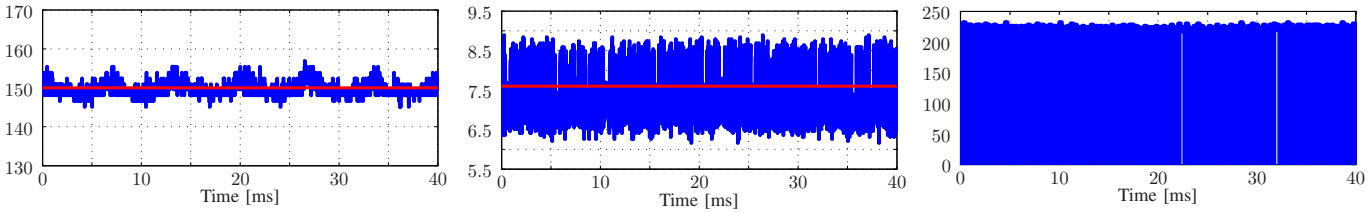

(a) Capacitor voltage v_{C_1} and its reference in [V] (b) Inductor current i_{L_1} and its reference in [A] (c) Dc-link voltage v_{dc} in [V]

Fig. 14: Experimental results of the dc side of the qZSI with MPC and an $1T_s$ prediction horizon length. The sampling interval is $T_s = 25\,\mu$s and $\lambda_u = 0.42$. The switching frequency is $f_{\text{sw}} \approx 5\,$kHz.

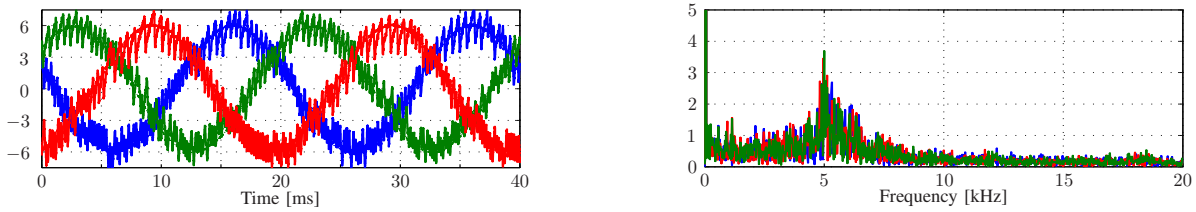

(a) Three-phase output current $\boldsymbol{i}_o$ (solid lines) and their references (dash-dotted lines) in [A] (b) Output current spectrum (%)

Fig. 15: Experimental results of the ac side of the qZSI with MPC and an $1T_s$ prediction horizon length. The sampling interval is $T_s = 25\,\mu$s and $\lambda_u = 0.42$. The switching frequency is $f_{\text{sw}} \approx 5\,$kHz and the output current THD $I_{o,\text{THD}} = 17.05\%$.

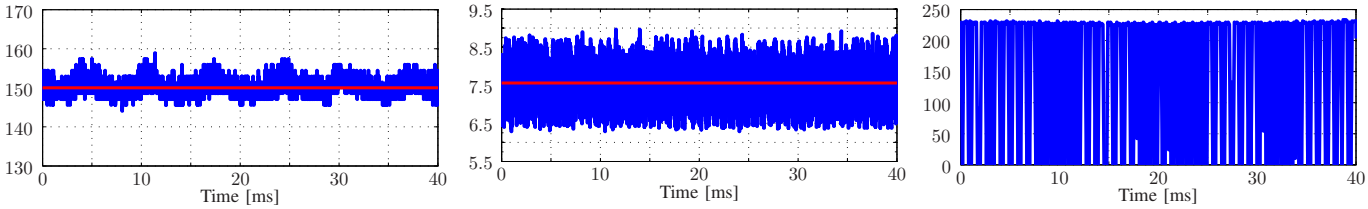

(a) Capacitor voltage v_{C_1} and its reference in [V] (b) Inductor current i_{L_1} and its reference in [A] (c) Dc-link voltage v_{dc} in [V]

Fig. 16: Experimental results of the dc side of the qZSI with MPC and a $5T_s$ prediction horizon length. The sampling interval is $T_s = 25\,\mu$s and $\lambda_u = 0.75$. The switching frequency is $f_{\text{sw}} \approx 5\,$kHz.

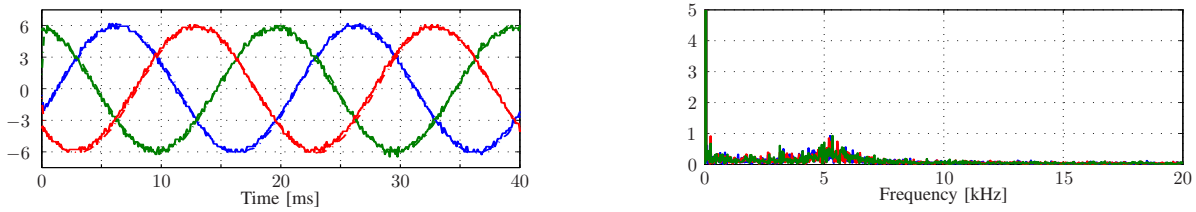

(a) Three-phase output current $\boldsymbol{i}_o$ (solid lines) and their references (dash-dotted lines) in [A] (b) Output current spectrum (%)

Fig. 17: Experimental results of the ac side of the qZSI with MPC and a $5T_s$ prediction horizon length. The sampling interval is $T_s = 25\,\mu$s and $\lambda_u = 0.75$. The switching frequency is $f_{\text{sw}} \approx 5\,$kHz and the output current THD $I_{o,\text{THD}} = 4.65\%$.

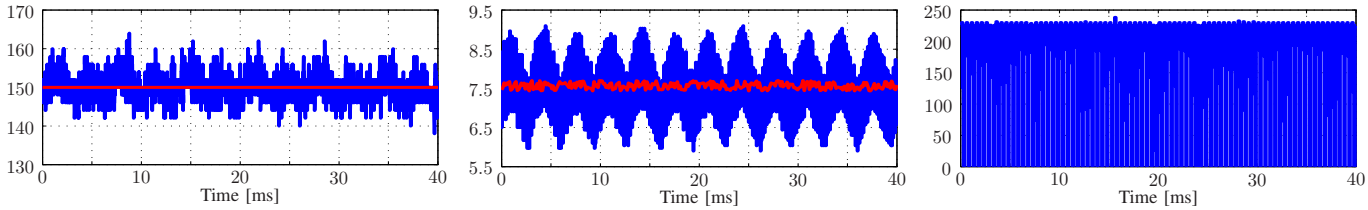

(a) Capacitor voltage v_{C_1} and its reference in [V] (b) Inductor current i_{L_1} in [A] (c) Dc-link voltage v_{dc} in [V]

Fig. 18: Experimental results of the dc side of the qZSI with PI-based control. The switching frequency is $f_{\text{sw}} = 5\,$kHz.

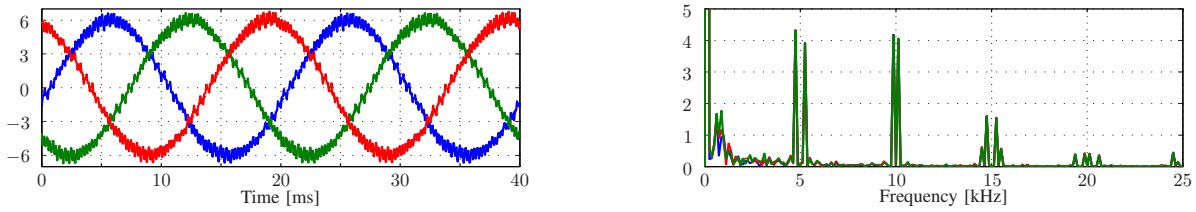

(a) Three-phase output current $\boldsymbol{i}_o$ (solid lines) and their references (dash-dotted lines) in [A] (b) Output current spectrum (%)

Fig. 19: Experimental results of the ac side of the qZSI with PI-based control. The switching frequency is $f_{\text{sw}} = 5\,$kHz and the output current THD $I_{o,\text{THD}} = 8.95\%$.

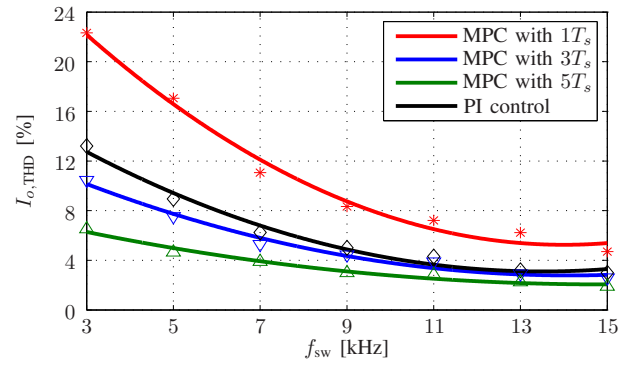

(a) Current THD and switching frequency.

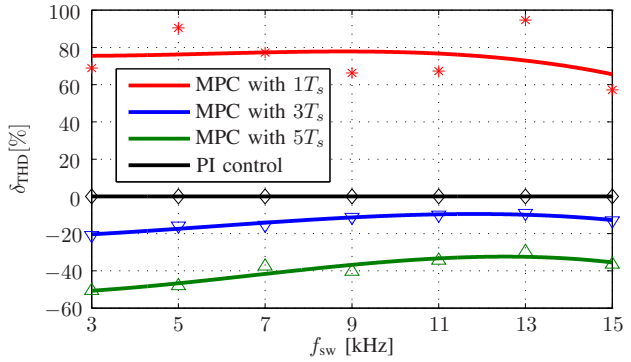

(b) Relative current THD and switching frequency.

Fig. 20: Trade-off between the output current THD $I_{o,\text{THD}}$ and the switching frequency f_{sw} for the PI-based controller and the MPC with prediction horizon length of $1T_s$, $3T_s$ and $5T_s$.

$3T_s$, and $5T_s$. For all cases examined, λ_u was appropriately tuned to obtain the desired switching frequency. The results with the MPC and the PI-based controller are illustrated in Fig. 20(a). Among the different prediction horizons, it can be noticed that the MPC with a $5T_s$ horizon introduces the lowest THD values over the whole range of the switching frequencies (from 3 up to 15 kHz). As can be seen, the resulting THD is lower than that produced by the linear controller (see Fig. 20(a)). Moreover, Fig. 20(b) displays the relative current THD. It can be concluded that the experimental results are in agreement with the respective simulation results presented in Section V-A.

C. Transient Response

The transient response of the proposed MPC strategy is examined with a $5T_s$ horizon and a switching frequency of 5 kHz. Again, for comparison purposes the transient performance of the PI-based controller is also scrutinized. The transient operation is examined in two cases: with step change in the output current reference and step change in the input dc voltage.

1) Step Change in the Output Current Reference : In this experiment, the desired output power $P_{o,\text{ref}}$ is stepped up from 135 to 540 W, thus the output current reference is stepped up from 3 A to 6 A. Accordingly, the inductor current reference changes from 1.9 A to 7.7 A ($i_{L_1,\text{ref}} = P_{o,\text{ref}}/v_{\text{in}}$). The dc- and ac-side results with the MPC are shown in Fig. 21, whereas the respective results with the linear controller are shown in Fig. 22.

As can be seen in Fig. 21(b), when MPC is employed, the inductor current tracks its reference both before and after the change in its reference value. Moreover, the capacitor voltage is kept constant to its reference value of 150 V (see Fig. 21(a)). It can be claimed that the proposed MPC offers a very good transient response with very short settling times for both the capacitor voltage and the inductor current. The dc side of the qZSI shows a good transient response when controlled with the linear control scheme, as well, see Fig. 22. However, in comparison with the proposed MPC, the PI-based controller shows slower transient response.

As for the ac side of the qZSI, both MPC and PI manage to eliminate the steady-state error (Figs. 21(c) and 22(c)). Nonetheless, MPC exhibits superior behavior during the transient.

2) Step Change in the Input dc Voltage: As previously mentioned, the qZSI proposes an attractive solution for the PV systems. In such a case, the resulting dc voltage from the PV is not constant, since it can change with the temperature and the solar radiation level during the day. In order to examine the performance of the proposed MPC strategy under such conditions, the input voltage is stepped up from 70 V to 100 V, while keeping the output current reference fixed at 6 A and the capacitor voltage reference at 150 V. In accordance with these settings, the inductor current reference changes from 7.7 A to 5.4 A, where $i_{L_1,\text{ref}} = P_{o,\text{ref}}/v_{\text{in}}$. The results of MPC and PI control are shown in Figs. 23 and 24, respectively.

As can be seen in Fig. 23(a), the capacitor voltage remains practically unaffected by this change in the input voltage, with only a small overshoot observed, whereas the inductor current quickly reaches its new reference value, see Fig. 23(b). The effectiveness of the proposed MPC is also verified by the ac-side result (Fig. 23(c)); as can be seen the output current exhibits very small fluctuations during the transient time. When the PI controller is employed, the ac-side response, shown in Fig. 23(c), is comparable with the one of the proposed MPC in terms of the time the transients lasts. However, the capacitor voltage displays a double overshoot and it takes longer time to return to its reference value, Fig. 24(a).

From the presented analysis, it can be concluded that the proposed long-horizon MPC has superior tracking abilities for all variables of concern, while it introduces zero steady-state error, low current THD, and very short transient times. These characteristics indicate an overall performance improvement of the qZSI.

VII. Conclusions

This paper proposes a long-horizon direct model predictive current control scheme for the quasi-Z-source inverter. To achieve an improved system performance, as quantified by the output current THD, as well as to ensure closed-loop stability, while controlling the switching frequency, long prediction horizons are required. However, in such a case enumeration of all candidate solutions becomes computationally prohibitive. To solve the underlying optimization problem in real time, a nontrivial prediction horizon—as resulted from a move blocking scheme—is implemented which, combined with a branch-and-bound technique, allows to keep the computational burden modest. The proposed techniques facilitate the implementation of a long-horizon MPC in an FPGA. The simulation and the experimental results verify the superior performance of long-prediction horizon MPC when compared to the existing one-step horizon MPC as well as to the established linear PI-based

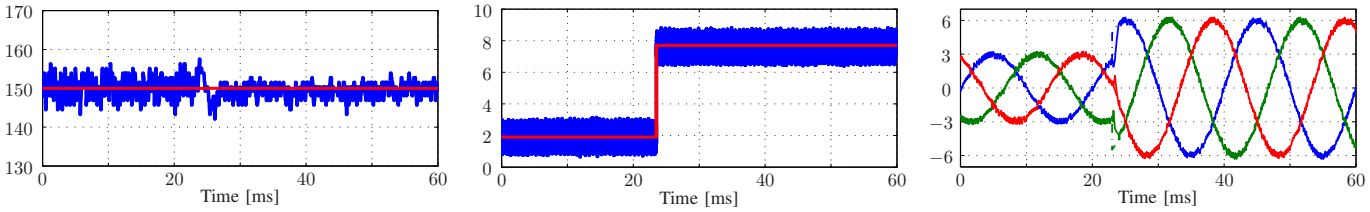

(a) Capacitor voltage v_{C_1} and its reference in [V] (b) Inductor current i_{L_1} and its reference in [A] (c) Three-phase output current $\boldsymbol{i}_o$ (solid lines) and their references (dash-dotted lines) in [A]

Fig. 21: Experimental results for a step change in the output current reference with MPC and a $5T_s$ prediction horizon length.

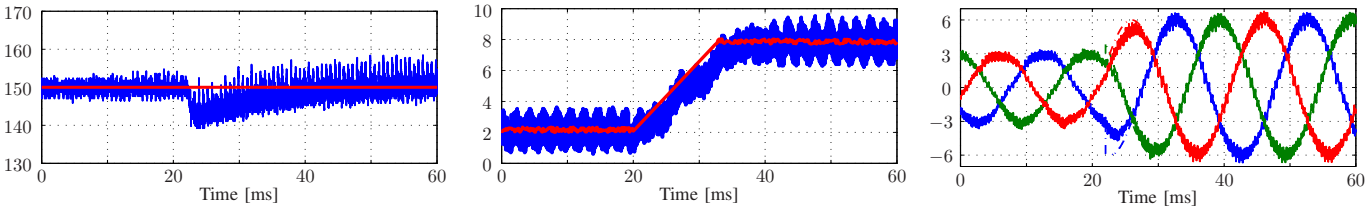

(a) Capacitor voltage v_{C_1} and its reference in [V] (b) Inductor current i_{L_1} in [A] (c) Three-phase output current $\boldsymbol{i}_o$ (solid lines) and their references (dash-dotted lines) in [A]

Fig. 22: Experimental results for a step change in the output current reference with a PI-based controller.

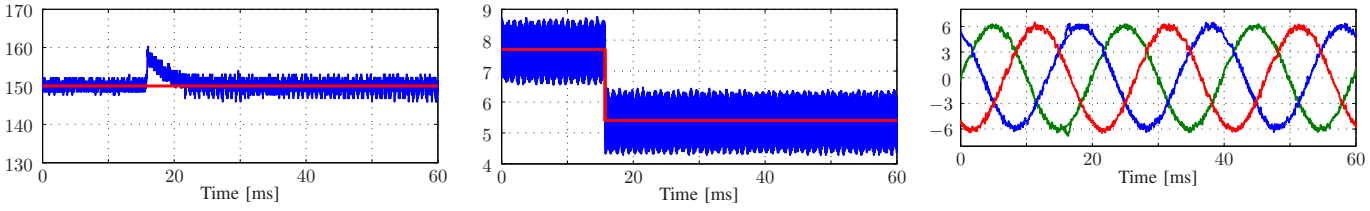

(a) Capacitor voltage v_{C_1} and its reference in [V] (b) Inductor current i_{L_1} and its reference in [A] (c) Three-phase output current $\boldsymbol{i}_o$ (solid lines) and their references (dash-dotted lines) in [A]

Fig. 23: Experimental results for a step change in the input dc voltage with MPC and a $5T_s$ prediction horizon length.

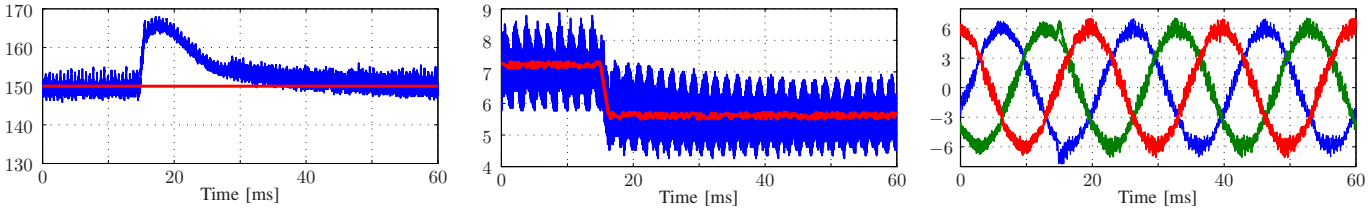

(a) Capacitor voltage v_{C_1} and its reference in [V] (b) Inductor current i_{L_1} in [A] (c) Three-phase output current $\boldsymbol{i}_o$ (solid lines) and their references (dash-dotted lines) in [A]

Fig. 24: Experimental results for a step change in the input dc voltage with a PI-based controller.

controller. More specifically, the proposed long-horizon direct MPC exhibits better steady-state behavior with lower output current THD, while, at the same time, it shows a much faster dynamic response on both sides of the qZSI.

Appendix A
Steady-State Analysis

At steady-state operation[11], and according to the inductor volt-second balance, the average voltage of the inductors is zero over one time window $T_1 = n_1 T_s$, with $n_1 \in \mathbb{N}^+$. Note that $T_1 \approx 1/f_{\text{sw}}$, with f_{sw} being the *average* switching frequency[12]. Therefore, the voltages of the capacitors C_1 and C_2, v_{C_1} and v_{C_2}, respectively, as well as the currents i_{L_1} and i_{L_2} of the inductors L_1 and L_2, respectively, are deduced as follows, assuming that $C_1 = C_2$ and $L_1 = L_2$

$$v_{C_1} = \frac{1-d}{1-2d} v_{\text{in}}\,, \quad v_{C_2} = \frac{d}{1-2d} v_{\text{in}}\,, \tag{14a}$$

$$i_{L_1} = i_{L_2} = \frac{1-d}{1-2d} i_{\text{load}}\,, \tag{14b}$$

where i_{load} is the load current as shown in Fig. 2(a). The *average* shoot-through duty cycle of the qZSI $d \in [0,\ 0.5)$ is defined as

$$d = \frac{T_0}{T_1} = \frac{n_0 T_s}{n_1 T_s} = \frac{n_0}{n_1}\,, \tag{15}$$

where T_0 is the time interval within the time window T_1 for which the load is short-circuited, i.e. the shoot-through time interval, and $n_0 < \frac{n_1}{2}$, $n_0 \in \mathbb{N}^+$. Moreover, the peak value of the dc-link voltage during the non-shoot-through period is

$$\hat{v}_{\text{dc}} = v_{C_1} + v_{C_2} = \frac{1}{1-2d} v_{\text{in}} = b v_{\text{in}} \tag{16}$$

where $b \geq 1$ is the boost factor resulting from the shoot-through period.

[11] In the analysis presented hereafter a variable switching frequency is considered, as is the case with the presented control algorithm.

[12] With MPC the switching frequency is variable and the *average* switching frequency is used to indicate the operating switching frequency of the converter.

APPENDIX B
PROPOSED CONTROL ALGORITHM

The proposed direct MPC algorithm for the qZSI is described in Algorithm 1. The initial values of the arguments are $\boldsymbol{U} = [\,]$, i.e. the empty vector, $\boldsymbol{x}(\ell) = \boldsymbol{x}(k)$, $\boldsymbol{u}_{abc}(\ell-1) = \boldsymbol{u}_{abc}(k-1)$, $J = 0$, $J^* = \infty$, $\ell = k$, and $m = 0$. Note that function f is the state-update function (7a), where the subscripts 1 and 2 correspond to the two different sampling intervals being used (T_s and T_s'), respectively, as explained in the move blocking strategy in Section III-D.

Algorithm 1 MPC algorithm

function $\boldsymbol{U}^*(k)$ = MPC($\boldsymbol{U}, \boldsymbol{x}(\ell), \boldsymbol{u}_{abc}(\ell-1), J, J^*, \ell, m$)
  for each $\boldsymbol{u}_{abc}(\ell) \in \boldsymbol{\mathcal{U}}$ **do**
    $\boldsymbol{U}_{3m+1:3(m+1)} = \boldsymbol{u}_{abc}(\ell)$
    if $\ell < k + N_1$ **then**
      $\boldsymbol{x}(\ell+1) = f_1(\boldsymbol{x}(\ell), \boldsymbol{u}_{abc}(\ell))$
    else
      $\boldsymbol{x}(\ell+1) = f_2(\boldsymbol{x}(\ell), \boldsymbol{u}_{abc}(\ell))$
    end if
    $\boldsymbol{y}_{\text{err}}(\ell+1) = \boldsymbol{y}_{\text{ref}}(\ell+1) - \boldsymbol{y}(\ell+1)$
    $\Delta\boldsymbol{u}_{abc}(\ell) = \boldsymbol{u}_{abc}(\ell) - \boldsymbol{u}_{abc}(\ell-1)$
    $J = J + ||\boldsymbol{y}_{\text{err}}(\ell+1)||^2_{\boldsymbol{Q}} + ||\Delta\boldsymbol{u}_{abc}(\ell)||^2_{\boldsymbol{R}}$
    if $J < J^*$ **then**
      if $\ell < k + N - 1$ **then**
        MPC($\boldsymbol{U}, \boldsymbol{x}(\ell+1), \boldsymbol{u}_{abc}(\ell), J, J^*, \ell+1, m+1$)
      else
        $J^* = J$
        $\boldsymbol{U}^*(k) = \boldsymbol{U}$
      end if
    end if
  end for
end function

REFERENCES

[1] A. Ayad, P. Karamanakos, and R. Kennel, "Direct model predictive current control of quasi-Z-source inverters," in *Proc. IEEE Int. Symp. Pred. Control of Elect. Drives and Power Electron.*, Valparaíso, Chile, Oct. 2015, pp. 1–6.

[2] F. Z. Peng, "Z-source inverter," *IEEE Trans. Ind. Appl.*, vol. 39, no. 2, pp. 504–510, 2003.

[3] Y. Huang, M. Shen, F. Z. Peng, and J. Wang, "Z-source inverter for residential photovoltaic systems," *IEEE Trans. Power Electron.*, vol. 21, no. 6, pp. 1776–1782, Nov. 2006.

[4] Y. Liu, H. Abu-Rub, and B. Ge, "Z-source/quasi-Z-source inverters: Derived networks, modulations, controls, and emerging applications to photovoltaic conversion," *IEEE Ind. Electron. Mag.*, vol. 8, no. 4, pp. 32–44, Dec. 2014.

[5] M. Shen, A. Joseph, J. Wang, F. Z. Peng, and J. Adam, "Comparison of traditional inverters and Z-source inverter for fuel cell vehicles," *IEEE Trans. Power Electron.*, vol. 22, no. 4, pp. 1453–1463, Jul. 2007.

[6] A. Battiston, J. Martin, E. Miliani, B. Nahid-Mobarakeh, S. Pierfederici, and F. Meibody-Tabar, "Comparison criteria for electric traction system using Z-source/quasi-Z-source inverter and conventional architectures," *IEEE J. Emerging Sel. Top. Power Electron.*, vol. 2, no. 3, pp. 467–476, Sept. 2014.

[7] J. Anderson and F. Peng, "Four quasi-Z-source inverters," in *Proc. IEEE Power Electron. Spec. Conf.*, Rhodes, Greece, Jun. 2008, pp. 2743–2749.

[8] F. Guo, L. X. Fu, C. H. Lin, C. Li, W. Choi, and J. Wang, "Development of an 85 kW bidirectional quasi-Z-source inverter with DC-link feedforward compensation for electric vehicle applications," *IEEE Trans. Power Electron.*, vol. 28, no. 12, pp. 5477–5488, Dec. 2013.

[9] B. Ge, H. Abu-Rub, F. Z. Peng, Q. Lei, A. de Almeida, and F. Ferreira, "An energy-stored quasi-Z-source inverter for application to photovoltaic power system," *IEEE Trans. Ind. Electron.*, vol. 60, no. 10, pp. 4468–4481, Oct. 2013.

[10] Y. Li, S. Jiang, J. Cintron-Rivera, and F. Z. Peng, "Modeling and control of quasi-Z-source inverter for distributed generation applications," *IEEE Trans. Ind. Electron.*, vol. 60, no. 4, pp. 1532–1541, Apr. 2013.

[11] A. Ayad, S. Hanafiah, and R. Kennel, "A comparison of quasi-Z-source inverter and traditional two-stage inverter for photovoltaic application," in *Proc. Int. Expo. and Conf. Power Electron., Intelligent Motion, Renew. Energy Management*, Nuremberg , Germany, May 2015, pp. 1–8.

[12] C. J. Gajanayake, D. M. Vilathgamuwa, and P. C. Loh, "Development of a comprehensive model and a multiloop controller for Z-source inverter," *IEEE Trans. Ind. Electron.*, vol. 54, pp. 2352–2359, Aug. 2007.

[13] O. Ellabban, J. Van Mierlo, and P. Lataire, "DSP-based dual-loop peak DC-link voltage control strategy of the Z-source inverter," *IEEE Trans. Power Electron.*, vol. 27, no. 9, pp. 4088–4097, Sept. 2005.

[14] J. Liu, S. Jiang, D. Cao, and F. Z. Peng, "A digital current control of quasi-Z-source inverter with battery," *IEEE Trans. Ind. Informat.*, vol. 9, no. 2, pp. 928–937, May 2013.

[15] J. Liu, S. Jiang, D. Cao, X. Lu, and F. Peng, "Sliding-mode control of quasi-Z-source inverter with battery for renewable energy system," in *Proc. IEEE Energy Convers. Congr. Expo.*, Phoenix, AZ, Sep. 2011, pp. 3665–3671.

[16] H. Rostami and D. A. Khaburi, "Neural networks controlling for both the dc boost and ac output voltage of Z-source inverter," in *Proc. Power Electron. Drive System Technology Conf.*, Feb. 2010, pp. 135–140.

[17] J. B. Rawlings and D. Q. Mayne, *Model Predictive Control: Theory and Design*. Madison, WI: Nob Hill, 2009.

[18] P. Cortés, M. P. Kazmierkowski, R. M. Kennel, D. E. Quevedo, and J. Rodríguez, "Predictive control in power electronics and drives," *IEEE Trans. Ind. Electron.*, vol. 55, no. 12, pp. 4312–4324, Dec. 2008.

[19] J. Rodríguez, M. P. Kazmierkowski, J. R. Espinoza, P. Zanchetta, H. Abu-Rub, H. A. Young, and C. A. Rojas, "State of the art of finite control set model predictive control in power electronics," *IEEE Trans. Ind. Informat.*, vol. 9, no. 2, pp. 1003–1016, May 2013.

[20] T. Geyer, "Low complexity model predictive control in power electronics and power systems," Ph.D. dissertation, Autom. Control Lab. ETH Zurich, Zurich, Switzerland, 2005.

[21] P. Karamanakos, "Model predictive control strategies for power electronics converters and ac drives," Ph.D. dissertation, Elect. Mach. and Power Electron. Lab. NTU Athens, Athens, Greece, 2013.

[22] W. Mo, P. Loh, and F. Blaabjerg, "Model predictive control for Z-source power converter," in *Proc. IEEE Int. Conf. Power Electron. and ECCE Asia*, May/Jun. 2011, pp. 3022–3028.

[23] M. Mosa, H. Abu-Rub, and J. Rodríguez, "High performance predictive control applied to three phase grid connected quasi-Z-source inverter," in *Proc. IEEE Indust. Elec. Society (IECON)*, Vienna, 2013, pp. 5812–5817.

[24] A. Ayad and R. Kennel, "Model predictive controller for grid-connected photovoltaic based on quasi-Z-source inverter," in *Proc. IEEE Int. Symp. Pred. Control of Elect. Drives and Power Electron.*, Munich, Germany, Oct. 2013, pp. 1–6.

[25] O. Ellabban, M. Mosa, H. Abu-Rub, and J. Rodríguez, "Model predictive control of a grid connected quasi-Z-source inverter," in *Proc. IEEE Indust. Tech. (ICIT)*, Feb. 2013, pp. 1591–1596.

[26] A. Ayad and R. Kennel, "Direct model predictive control of quasi-Z-source inverter compared with the traditional PI-based PWM control," in *Proc. Eur. Power Electron. Conf.*, Geneva, Switzerland, Sep. 2015, pp. 1–9.

[27] A. Bakeer, M. Ismeil, and M. Orabi, "A powerful finite control set-model predictive control algorithm for quasi Z-source inverter," *IEEE Trans. Ind. Informatics*, vol. 12, no. 4, pp. 1371–1379, May 2016.

[28] M. Mosa, R. Balog, and H. Abu-Rub, "High performance predictive control of quasi impedance source inverter," *IEEE Trans. Power Electron.*, doi: 10.1109/TPEL.2016.2531989, to appear.

[29] S. Bayhan, H. Abu-Rub, and R. S. Balog, "Model predictive control of quasi-Z-source four-leg inverter," *IEEE Trans. Ind. Electron.*, vol. 63, no. 7, pp. 4506–4516, Jul. 2016.

[30] T. Geyer and D. Quevedo, "Multistep finite control set model predictive control for power electronics," *IEEE Trans. Power Electron.*, vol. 29, no. 12, pp. 6836–6846, Dec. 2014.

[31] T. Geyer, P. Karamanakos, and R. Kennel, "On the benefit of long-horizon direct model predictive control for drives with LC filters," in *Proc. IEEE Energy Convers. Congr. Expo.*, Pittsburgh, PA, Sep. 2014, pp. 3520–3527.

[32] T. Geyer and D. Quevedo, "Performance of multistep finite control set model predictive control for power electronics," *IEEE Trans. Power Electron.*, vol. 30, no. 3, pp. 1633–1644, Mar. 2015.

[33] J. Rodríguez and P. Cortés, *Predictive control of power converters and electrical drives*. West Sussex, UK: John Wiley & Sons, 2012.

[34] E. L. Lawler and D. E. Wood, "Branch-and-bound methods: A survey," *Op. Res.*, vol. 14, no. 4, pp. 699–719, Jul./Aug. 1966.

[35] R. Cagienard, P. Grieder, E. C. Kerrigan, and M. Morari, "Move blocking strategies in receding horizon control," *J. of Process Control*, vol. 17, no. 6, pp. 563–570, Jul. 2007.

[36] P. Karamanakos, T. Geyer, and S. Manias, "Direct voltage control of dc-dc boost converters using enumeration-based model predictive control," *IEEE Trans. Power Electron.*, vol. 29, no. 2, pp. 968–978, Feb. 2014.

[37] P. Karamanakos, T. Geyer, N. Oikonomou, F. D. Kieferndorf, and S. Manias, "Direct model predictive control: A review of strategies

that achieve long prediction intervals for power electronics," *IEEE Ind. Electron. Mag.*, vol. 8, no. 1, pp. 32–43, Mar. 2014.
[38] F. Z. Peng, M. Shen, and Z. Qian, "Maximum boost control of the Z-source inverter," *IEEE Trans. Power Electron.*, vol. 20, no. 4, pp. 833–838, 2005.
[39] L. P. Chiang, F. Blaabjerg, and W. C. Pang, "Comparative evaluation of pulse-width modulation strategies for Z-source neutral-point-clamped inverter," *IEEE Trans. Power Electron.*, vol. 22, no. 3, pp. 1005–1013, 2007.
[40] P. Cortés, J. Rodríguez, C. Silva, and A. Flores, "Delay compensation in model predictive current control of a three-phase inverter," *IEEE Trans. Ind. Electron.*, vol. 59, no. 2, pp. 1323–1325, 2012.

Ayman Ayad (S'13) was born in Menia, Egypt, in 1984. He received the B.S. degree in electronic engineering and the M.Sc. degree in automatic control from Menofia University, Menofia and Cairo University, Giza, Egypt, in 2006 and 2009, respectively.

From 2007 to 2011, he was a teaching assistant in the department of Electrical and Computer Engineering, Sinai University, Al-Arish, North Sinai, Egypt. Since November 2011, he has been working toward his Ph.D. at the Chair of Electrical Drive Systems and Power Electronics, Technische Universität München, Munich, Germany. His research interests include power electronic converters, model predictive control, and renewable energy systems.

Petros Karamanakos (S'10—M'14) received the Diploma and the Ph.D. degrees in electrical and computer engineering from the National Technical University of Athens (NTUA), Athens, Greece, in 2007, and 2013, respectively.

From 2010 to 2011, he was with the ABB Corporate Research Center, Baden-Dättwil, Switzerland, where he worked on model predictive control strategies for medium-voltage drives. From 2013 to 2016, he was a PostDoc Research Associate in the Chair of Electrical Drive Systems and Power Electronics, Technische Universität München, Munich, Germany. He is currently an Assistant Professor in the Department of Electrical Engineering, Tampere University of Technology, Tampere, Finland. His main research interests lie at the intersection of optimal control, mathematical programming and power electronics, including model predictive control for power electronic converters and ac drives.

Dr. Karamanakos received the 2014 Third Best Paper Award of the IEEE Transactions on Industry Applications and the First Prize Paper Award of the Industrial Drives Committee at the 2013 IEEE Energy Conversion Congress and Exposition.

Ralph Kennel (M'89—SM'96) received the Diploma and the Dr.-Ing. degrees from the University of Kaiserslautern, Kaiserslautern, Germany, in 1979 and 1984, respectively, for his work on the application of model predictive control in power electronics.

From 1994 to 1999, he was a Visiting Professor at the University of Newcastle-upon-Tyne, Tyne and Wear, U.K. From 1999 to 2008, he was a Professor with the Faculty of Electrical Machines and Drives, Wuppertal University, Wuppertal, Germany. Since 2008, he has been a Professor with the Chair of Electrical Drive Systems and Power Electronics, Technische Universität München, Munich, Germany. His research interests include sensorless control of ac drives, predictive control of power electronics, and hardware-in-the-loop systems.

Prof. Kennel is a Chartered Engineer in the U.K. Within the IEEE, he is the Treasurer of the Germany Section as well as Distinguished Lecturer of the Power Electronics Society (IEEE-PELS). He has received in 2013 the Harry Owen Distinguished Service Award from IEEE-PELS as well as the EPE Association Distinguished Service Award in 2015. In addition, Prof. Kennel was appointed Extraordinary Professor by the University of Stellenbosch (South Africa) from 2016 to 2019 and as Visiting Professor at the Haixi Institute by the Chinese Academy of Sciences from 2016 to 2021.